

# Deep Learning for Void Detection in Composite Oriented Strand Board

Wenyue Hu<sup>1</sup>, Xiaoxing Wang<sup>2</sup>, Christopher C. Bowland<sup>3</sup>, Phu Nguyen<sup>4</sup>, Carina Xiaochen Li<sup>5</sup>,  
Steven Nutt<sup>1</sup>, Bo Jin<sup>1</sup>

<sup>1</sup> M.C. Gill Composites Center, University of Southern California

<sup>2</sup> MathWorks Japan

<sup>3</sup> Chemical Sciences Division, Carbon and Composites Group, Oak Ridge National Lab

<sup>4</sup> The Gill Corporation, El Monte, California

<sup>5</sup> Necstlab, Department of Aeronautics and Astronautics, Massachusetts Institute of Technology

## ABSTRACT

X-ray micro-computed tomography (micro-CT) offers the ability to assess and quantify microstructural characteristics in general, and the distribution of voids in particular, in composite laminates. Despite these capabilities, analysis of micro-CT data generally requires extensive training and human input regarding detection, number counting, morphology analysis, and predictions of mechanical performance. In recent years, advances in Deep Learning (DL) have been applied to challenging tasks of image processing, such as automatic detection and analysis of features in images, and rapid classifications of features with minimal human intervention/oversight. The application of DL simplifies the pipeline of tomography analysis by automating void detection and segregation, providing an accessible path to in-depth studies of porosity evolution.

This study describes an automated void segmentation solution built within commercial software (MATLAB) and applied to cross-sectional scans of Composite Oriented Strand Board (COSB). By training labeled data produced by grayscale binary masking, three of the most representative neural networks are assessed, based on the respective performance and accuracy in void detection. A Fully Convolutional Network (FCN, a neural network) performed semantic segmentation at the pixel level. A modified FCN, SegNet, was created by making the encoder-decoder structure symmetrical. The third FCN, U-net (used in biomedical image segmentation), was thought to be the state-of-art segmentation solution. Compared with the manual-labeled dataset, FCN, which yields the most accurate results statistically and successfully incorporates boundary-aware segmentation, outperformed the other two networks. Furthermore, FCN could be combined with pre-processing binary masking to develop an autonomous annotation tool for void-content study. SegNet was intended for scene understanding and therefore falsely occupied a larger area than the labeled ground truth voids, while U-net exhibited limitations in continuous boundary depiction when irregularities and perturbations were engaged.

## 1. INTRODUCTION

This study describes a fully automated, robust segmentation tool to replace human-performed void identification in carbon fiber reinforced polymers (CFRPs), particularly composite oriented strand board (COSB). Grayscale-based binary masking was first implemented to classify and label micro-CT scans of COSB cross-sections. Using labeled data as input, we down-selected the Neural Network (NN) that yields the most accurate results to human-labeled data among three semantic

segmentation solutions, namely Fully Convolutional Network (FCN), SegNet, and U-net, to replicate and exceed human performance in void-segmentation. In addition, the manufacturing of COSB and the use of micro-CT are discussed in the data acquisition process.

The application and demand for CFRPs have increased steadily in the aerospace, defense, automotive, and wind energy industries because of superior mechanical performance levels, low density, durability, and resistance to fatigue and corrosion. In 2020, the CFRP market was valued at 7 billion dollars and had a market share of 45% of the composites market; an annual growth rate of 8.3% was forecast from 2021 to 2030, reaching 15.4 billion dollars by 2030. Voids in CFRPs are considered undesirable defects that stem from the manufacturing process. They can degrade a broad range of mechanical properties, such as interlaminar shear stress, but usually remain hidden and undetected [1]. Researchers are increasingly interested in investigating porosity evolution. By understanding the evolution and distribution of porosity, researchers can limit/eliminate formation by modifications to the manufacturing process, such as optimizing cure parameters (pressure, temperature, duration, etc.) and protocols, and designing processes and materials that restrict void formation and growth. Presently, most void detection/measurement and quantification are performed by trained professionals, causing a heavy burden of time, labor, and cost. To reduce this burden and respond to the growing sector, autonomous analysis solutions are needed and offer approaches to increasing automation in manufacturing [14 - 18].

In general, the voids study is divided into two steps. First, tomography is used to detect porosity in CFRPs through C-scan visualization of porous regions (lower density). Second, human experts intervene to identify and assess void morphology, location, volume fraction, and distribution. However, because of the large file sizes of micro-CT data, manual identification and evaluation require onerous human input and time. Computer vision and deep learning have the capability to extract information from tomographs and to inspect the material quality. In recent years, these tools have been refined to offer faster computation and more in-depth analysis. Automated detection is replacing the second step of the void analysis, with promising results in different fields, including composites. Wei et al. trained convolutional neural networks (CNN) architecture using small sample sizes but still generate more accurate results than some of the conventional machine learning algorithms such as k-nearest neighbor (KNN) and support vector machines (SVM) [4]. Among these NNs, the NN for semantic segmentation, which classifies parts of images at pixel-level, yields the most accurate results for small-scale analysis like cross-sections of composites. Kopackzka et al. used U-net and ConvNet by first segmenting the fabric images into subtypes before a set of specialized descriptors was indicated to help with pixel-level classification [7]. Fully Convolutional Network (FCN) integrates three conventional classification networks, VGG net, AlexNet, and GoogLeNet, producing state-of-art semantic segmentation results in the online data challenge PASCAL VOC in 2015, with the shortest inference time by then [11]. SegNet, which specializes in all layers serving semantic segmentation, yields high accuracy in large-size and high-resolution images [12]. However, these studies focused only on a small scale of data, leaving a question mark for the validation of these NNs if the dataset is more complex and larger scaled.

In this work, micro-CT was used to capture cross-sections of COSB. Using a method to stitch multiple scanned volumes, each three-dimensional micro-CT tomography yielded more than 150 two-dimensional images, comprising a dataset of ~2000 images. To label this dataset manually would be prohibitively time-consuming. Therefore, we applied binary grayscale-based masking, a conventional technique widely used in image analysis, to the training portion of the dataset. Grayscale-based segmentation is widely used in image processing software (such as ImageJ), as

well as in the micro-CT post-scanning data analysis. The binary masking technique automatically labeled the entire dataset in less than a half-second per image and required little human intervention.

This study combines conventional grayscale masking and deep learning neural networks in a new void segmentation approach. Binary-masked images were used as the input training dataset. The Neural Network, which, among FCN, SegNet, and U-net, yielded results closest to trained professionals and out-performed other models [3, 9, 10]. The objectives of this study are listed below and in Figure 1.

1. Produce COSBs using two layup methods (mat-stacking and mechanical agitation) and prepreg scraps  $10 \times 20$  mm and  $10 \times 100$  mm.
2. Use micro-CT imaging to obtain the cross-section images of the COSBs.
3. Investigate three neural networks: Fully Convolutional Networks (FCN), SegNet, and U-net, for semantic segmentation to automate the porosity detection in cross-sectional imaging.
4. Compare the training results with manual-labeled ground truth to determine the accuracy of each network.
5. Identify the best-performed model, which has the greatest potential for a fully automated segmentation tool to replicate human-performed void identification.

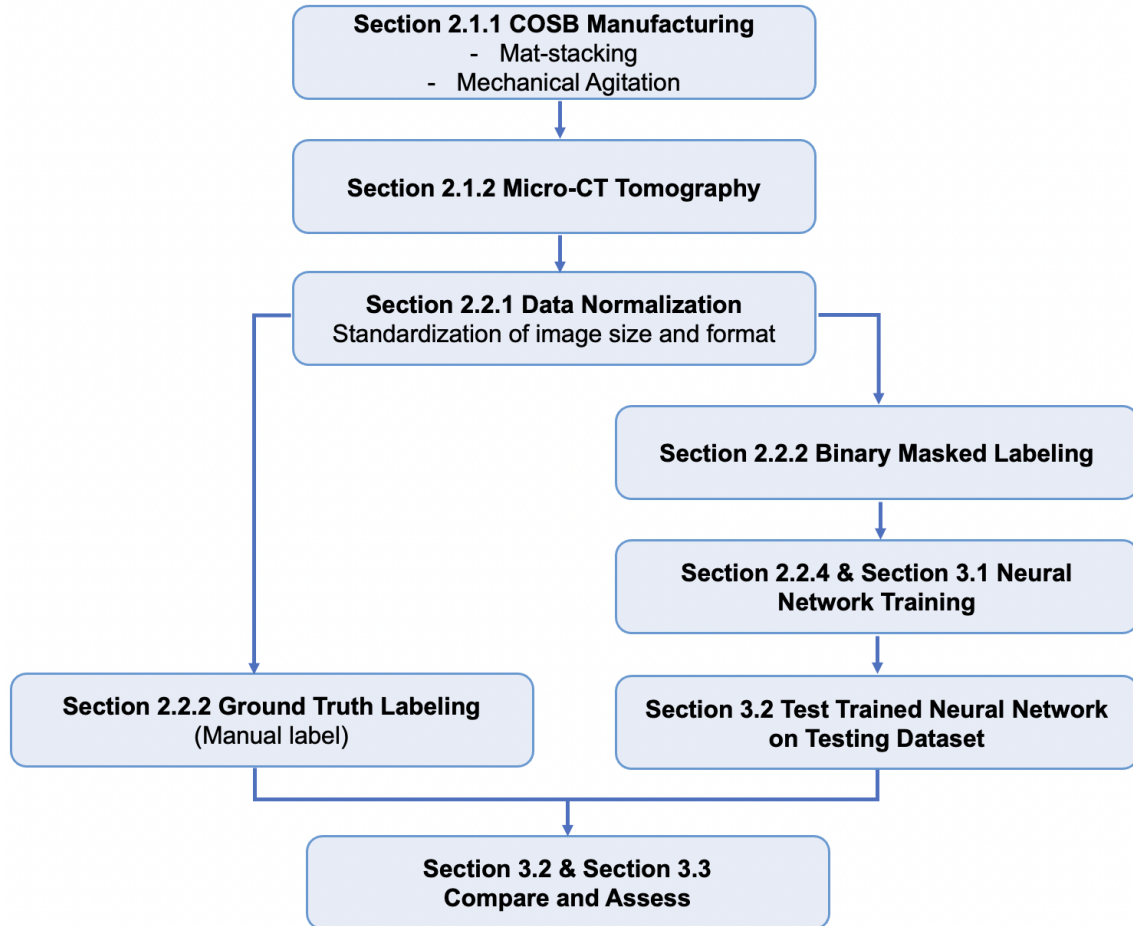


**Figure 1.** Logic flow and main objectives of this paper:  
to develop a fully automated and robust void segmentation tool

## 2. EXPERIMENTATION

### 2.1 Data Gathering

Panels of composite-oriented strand board (COSB) were produced from fresh unidirectional carbon fiber-epoxy prepreg strands [9]. Two types of layup methods were used in the manufacturing process - mat-stacking and mechanical agitation layups. Void content and morphology were investigated using microscopy of polished cross-sections and stitched high-resolution micro-CT images.

#### 2.1.1 Manufacturing of COSB

A demonstrator COSB panel was produced first. Fresh prepreg (UD Tape T40/800B with Cytec CYCOM 5320-1 Epoxy Resin) was cut into rectangular strands 10 mm  $\times$  20 mm (Figure 2) and distributed evenly on an aluminum plate. The prepreg was cured by compression molding (Wabash hot press) into a flat COSB panel measuring 215.9 mm  $\times$  215.9 mm. The panel is analogous to the ubiquitous wood-based oriented strand board (OSB, Figure 2). A CNC milling machine with a diamond cutting wheel was used to section the COSB into seven plain tensile coupons (25 mm  $\times$  200 mm) per ASTM D3039 standard for quasi-static tensile testing. Six coupons were tested in a load frame (INSTRON), and elastic modulus was determined from the load-displacement curves. One coupon prepared from the center of the COSB was cut into smaller pieces (25mm by 50mm) for non-destructive evaluation (NDE) using high-resolution micro-CT.

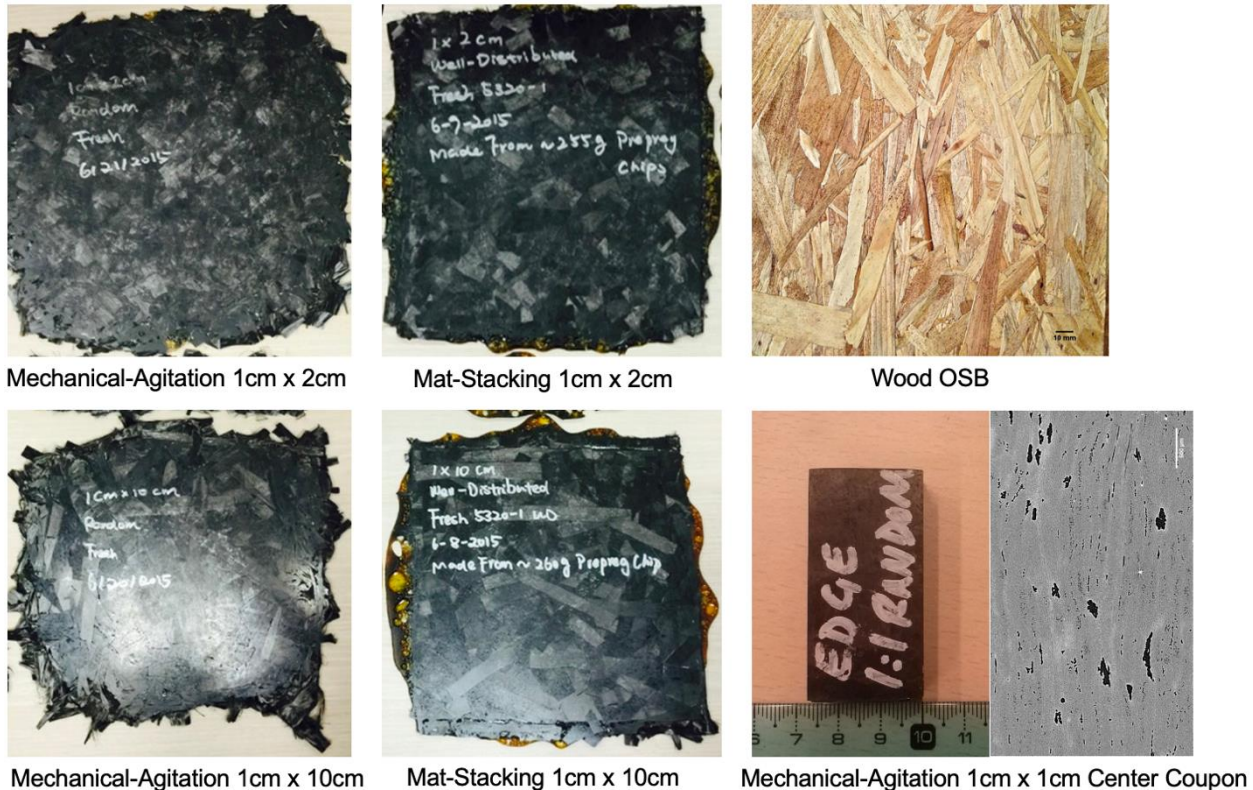


**Figure 2.** Left 4 images: COSB made of prepreg strands of 2 sizes and 2 layup methods.

Upper right image: Wood OSB, for reference.

Lower right image: the Micro-CT sample of the 1cm x 1cm Mechanical-Agitation COSB, and a 2-D micro-CT image (resolution: 2.5  $\mu$ m/px).



### 2.1.2 Micro-CT Analysis

X-ray computed can be used for 3D image reconstruction to detect defects (micro-cracks, inclusions, voids, delamination, and debonding), determine the distribution of mass, and accurately measure and display internal structural configurations. Previous studies [11] have indicated that the resolution of micro-CT is well-suited to the detection of internal and surface defects in carbon fiber epoxy composites. In this work, a tomographic machine (Phoenix Nanotom, General Electric) with a Hamamatsu C-7942 detector and a Mo anode was used to perform micro-CT scans on the demonstrator COSB. A micro-CT sample ( $25 \times 50 \times 3$  mm, Figure 2 lower right image) was prepared from the center of the panel. Electric tensions between 30 kV and 55 kV and current intensities between 190  $\mu$ A and 220  $\mu$ A were used. Spatial resolutions between 2.5  $\mu$ m/px and 14.5  $\mu$ m/px were attained from the above setup.

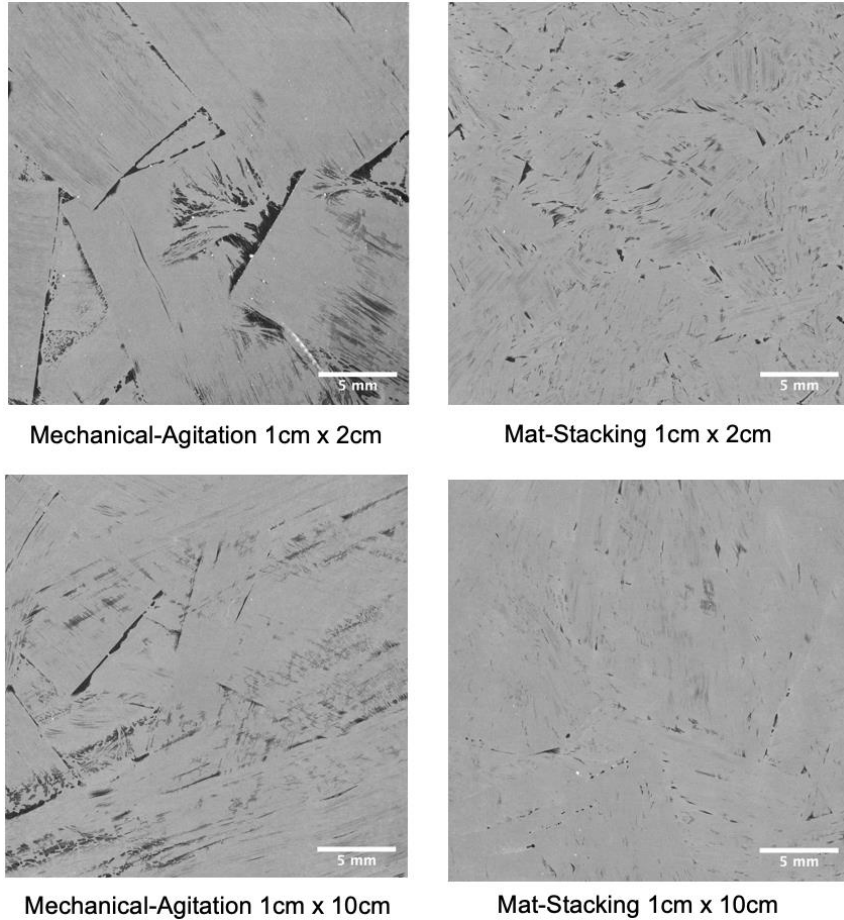


**Figure 3.** Micro-CT scans of COSBs made of prepreg strands of 2 sizes and 2 layup methods.

Initial scans showed that clear boundaries between strands could not be resolved, even at the highest resolution. However, when viewing continuous frames of scanned images, an animation reveals strand boundaries. This finding was helpful in identifying shapes of deformed strands and stitching multiple volumes for further post-processing and analysis. The technique was also useful for estimating void content. Thus, all samples were scanned in sets of 3-4 simultaneous samples to optimize available tomograph time. Updated settings were 80 kV and 150  $\mu$ A, with a 500 ms exposure time, and the attained resolution was 13.04  $\mu$ m/px.

Multiple scans were performed on different regions of a single sample to cover the entire sample volume. The volumes obtained were reconstructed using a user-defined routine. By stitching and cropping, an individual volume containing the complete sample volume was obtained, and the results appear in Figure 4. In the demonstrator COSB comprised of fresh prepreg strands, voids appear as needle shapes, and void content was 8.6%. This value is greater than the 2.1% void content determined via microscopic analysis of polished sections. This is not surprising, as the void content from micro-CT is obtained from a 3-D volume, while the void content determined from light microscopy is obtained from 2-D images. There is a difference of one spatial degree between the two sources of data. 3D void information obtained via micro-CT has advantages compared to 2-D information obtained from light microscopy of polished sections.

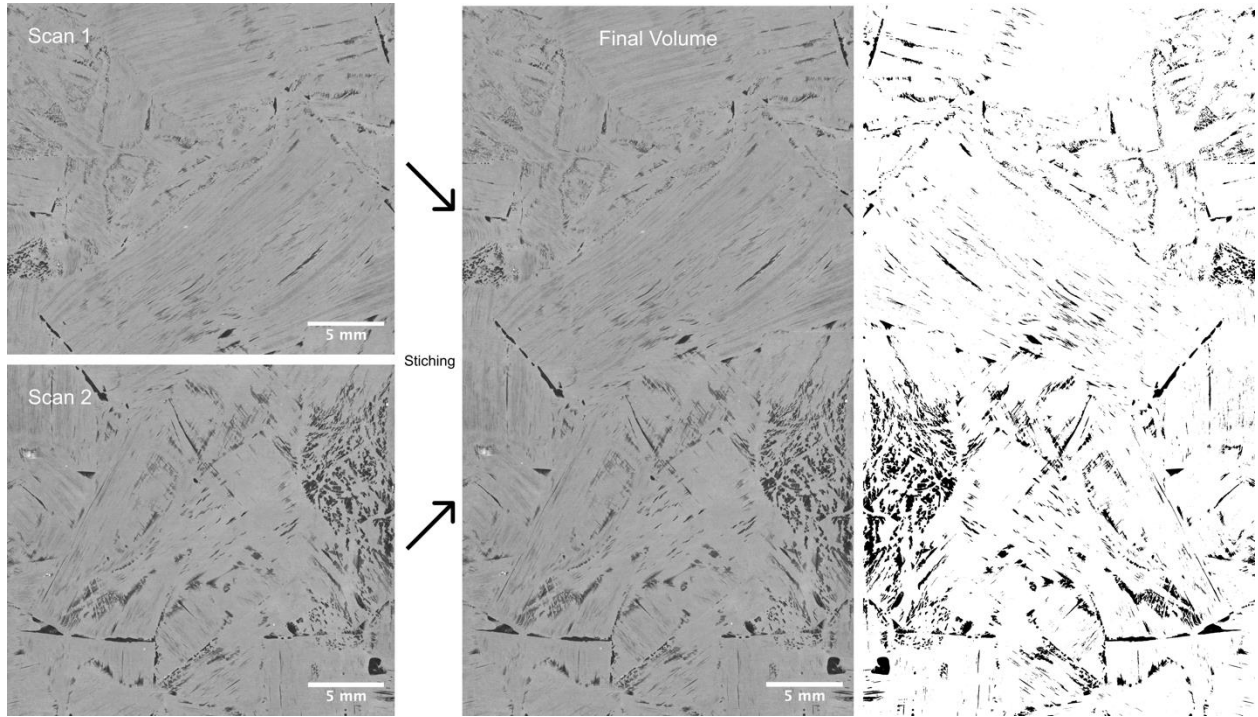


**Figure 4.** Stitching of multiple scanned volumes to obtain completed final micro-CT scanned volume.

The micro-CT dataset included 1925 images from four COSB panels using 2 layup methods (mechanical agitation, and mat-stacking) produced with two prepreg strand aspect ratios (1:2 and 1:10). The resolution of each image was  $>3400$  by 1900 pixels, and the entire dataset occupied  $\sim 12$ GB of memory. Due to the limited storage space and micro-CT sample size, a global view of void distribution at the panel level was not obtainable. To accommodate this limitation, images were stitched together, making it an animation-like continuous frame, which representatively and accurately characterized the prepreg strands and void content.

## 2.2 Deep Learning Algorithmic Pipeline and Implementation

### 2.2.1 Data Normalization (Pre-Processing)

Due to the different resolutions of the images, basic preprocessing is required to achieve data uniformity. The raw data is three-dimensional, stored in an uncompressed image file type

(RAW format) that captures detailed information received from the signal sensors. As only two-dimensional image analysis was performed in this study, we used a Java-based image processing tool (Image J), to transform RAW-format data into high-quality two-dimensional graphics with slightly different resolutions in TIF format. For example, as shown in Table 1, if the original data structure was  $1900 \times 3480 \times 115$  pixels, this was converted to 115 images in  $1900 \times 3480$  pixels resolution.

**Table 1.** Summary of the dataset structure. A: mechanical agitation, B: mat-stacking layup.

<b>Dataset Name (mm)</b>	<b>Data Structure (pixels)</b>	<b>File Format</b>	<b>Transformed Image Size (pixels)</b>	<b># Of Images</b>
Group A, 10x20	Center: 1900×3480×115 Edge: 1905×3450×250	RAW	Center: 1900×3480 Edge: 1905×3450	Center: 115 Edge: 250
Group A, 10x100	Center: 1905×3460×230 Edge: 1905×3500×230	RAW	Center: 1905×3460 Edge: 1905×3500	Center: 230 Edge: 230
Group B, 10x20	Center: 1910×3450×230 Edge: 1910×3460×225	RAW	Center: 1910×3450 Edge: 1910×3460	Center: 230 Edge: 225
Group B, 10x100	Center: 1900×3470×315 Edge: 1900×3500×330	RAW	Center: 1900×3470 Edge: 1900×3500	Center: 315 Edge: 330

Among the three neural networks, only FCN accepted different input data sizes as training input. Thus, to maintain the fairness of the experiments, images were resized to a uniform resolution of  $3400 \times 1900$  pixels. The study presented two types of labeling: manual labeling to serve as the ground truth, while binary masked labels were used for training neural networks.

### 2.2.2 Ground Truth Labeling

Ground truth is the accurate reference for deep learning training results. Human-generated labeled data, based on direct observation and measurement, was used as ground truth to compare with auto-generated pixel labels using neural networks. An app (MATLAB Image Labeler) was used to label randomly selected datasets manually. Various shapes and tools can mark a region of interest (ROI). In this case, pixel-level ROI labels were generated using a  $2 \times 2$  pixels brush and a second tool (Flood Fill) for larger areas. As shown in Figure 5, the labeler app enables users to outline the shape of ROIs and match them with user-defined classes (void and panel). A specified color represents each class, so labeled images are readily distinguishable. At the end of the labeling process, the labels and definitions were exported as a unit-8 pixels label matrix and a MAT-file. Ground truth data were stored and compared with results from the neural network training.

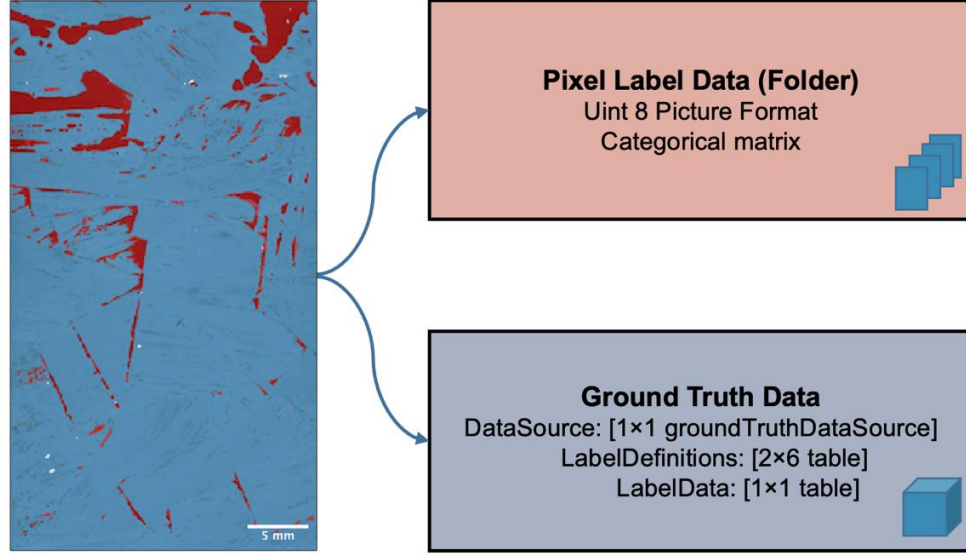


**Figure 5.** Manual labeling process using MATLAB Image Labeler app. The labeling process exported an unsigned integer (uint) 8 pixels label matrix and the ground truth data.

### 2.2.3 Binary Masking for Input Data

Labeling and masking techniques were used based on binary-grayscale thresholding to parse the void content from other parts of the tomographs. This technique relies on the difference in grayscale intensities of the void and the panel. Due to the different attenuation of X-rays from regions of different densities and atomic numbers, the high-density portion of the panel (fiber) appeared brighter than the low-density portions (voids) [13], allowing the application of binary masking. The accuracy of binary masking depends on the cleanness of boundaries between objects, the size of the objects, and the connectivity parameter [3]. Voids appear dark, with clear boundaries and distinct intensities from neighbors. As shown in Figure 6, voids were identified and labeled yellow after the binary masking process.

In general, the binary-threshold masking process of one image consists of six steps. Control flow statement such as for-loop was used for batch processing the entire dataset.

Step1: Display the original, unlabeled image.

Step 2: If a panel and background exist, use a morphological structuring function to define the boundary of the panel.

Step 3: Exclude the background and only show the panel's content.

Step 4: Mask the image based on binary thresholding (voids were labeled when larger than the mean intensity, and vice versa). Now, the ROI of the panel was defined.

Step 5: Repeat step 4 but blacken the inside region. Now, the ROI of the void was defined.

Step 6: Display labeled voids over the original image.



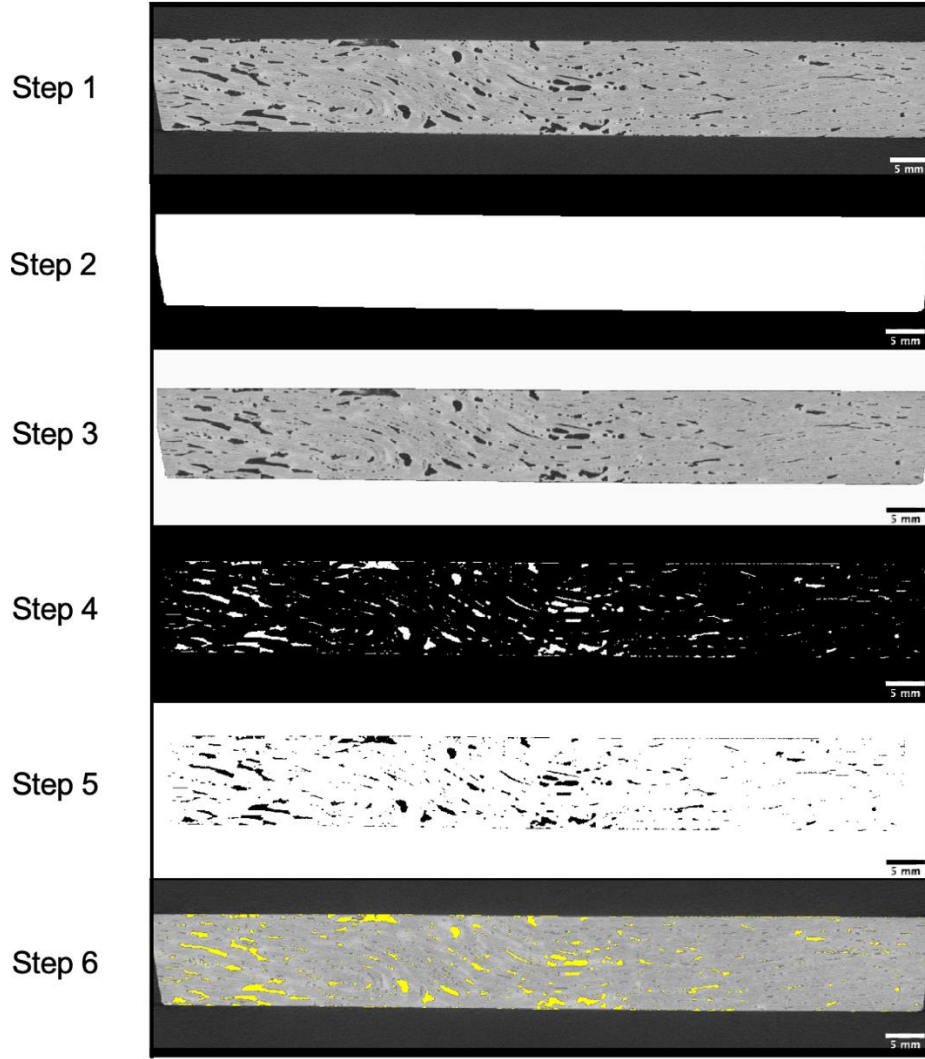


**Figure 6.** General 6-steps-process of binary grayscale masking of an image. Voids and panel areas were identified, separated, and labeled throughout the process.

#### 2.2.4 Setting of Three Neural Networks

MATLAB was used in assisting data analysis and training neural networks. The dataset with a total of 1925 images has been randomly partitioned based on the 60/40 Training and Testing portion, which means there are 1155 images in the training dataset (60%) and 770 images in the testing dataset (40%). Each neural network was trained by the binary-masked training dataset and performed void segmentation independently on the testing dataset. Recognizing that the deep learning training process requires a considerable amount of input data, long process time, and significant computational power, a workstation with GPU installed was implemented for all the training experiments. To compare the elapsed time of each neural network, all were trained in the same environment.

Data augmentation, the technique of expanding the dataset size, was applied only to U-net. This was because the neural networks were trained not only for the pixel intensity but also for localization and morphology. Flipping or adding noise to data augmentation might adversely affect

the training dataset, leading the unprecise predicted results. In addition, FCN and SegNet are believed to be unresponsive to image enhancement methods such as mirroring and dithering. Therefore, we attempted to make the original dataset more diverse in voids morphology and distribution to produce satisfactory results and avoid data augmentation in FCN and SegNet.

### 3. RESULTS AND DISCUSSION

#### 3.1 Training Process of Three Neural Networks

Two quality metrics - accuracy and loss values - were introduced to assess the progression of the training process of each network by iteration. Accuracy is a ratio between the number of correct predictions and the total number of predictions, indicating the overall performance of all classes, weighting them as equally important. Conversely, loss values quantify the unoptimized problems and errors of any machine to a number, reflecting on processes and parameters that can be improved. We had an imbalanced dataset where one of the classes, “panel”, occupied more than half of the content in the imaging dataset, and this made accuracy prone to higher scores. Thus, loss values provided a more comprehensive indicator for monitoring the training process. As shown in Figure 7, all three loss functions decreased monotonically with a number of iterations, indicating that the models were robust and increased in accuracy with a number of iterations.

FCN Training Dataset: the FCN was initially trained with 30 epochs. However, the training statistics indicated that fewer epochs were required since, after the 300<sup>th</sup> iteration, the accuracy percentage was essentially constant. Training with excess epochs can lead to over-fitting the dataset, such that the network memorizes the images but not the characteristics and labels of pixels. Therefore, 10 epochs were performed with the training dataset to reduce computational time.

SegNet Training Dataset: each image was divided into 10 patches to save GPU computational power while not characterizing random noise into underlying relationships to underfit the data. Due to limited time constraints, only 10 epochs were performed.

U-net Training Dataset: U-net welcomes various image enhancement methods; therefore, data augmentation of rotation of 90 degrees, 180 degrees, and 270 degrees were applied. Each image was divided into 50 patches to save GPU memory while not underfitting the data. 10 epochs and >40,000 iterations were performed, spending 230 minutes training the network. The training progress was recorded for the optimized parameters for the network (Figure 7 and Table 2).

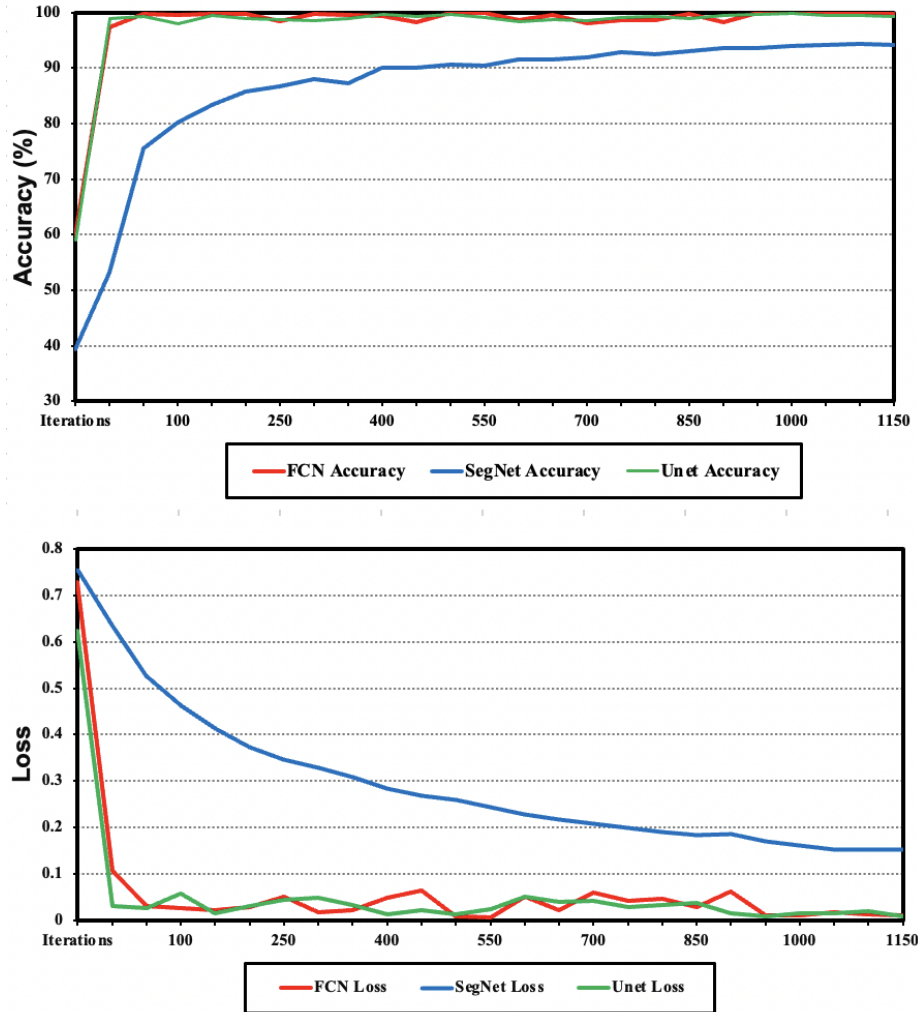


**Figure 7.** Training progress during the first epoch. Accuracy against iterations during the first epoch of FCN, SegNet, and U-net training progress (upper). Loss against iterations during the first epoch of FCN, SegNet, and U-net training progress (lower).

**Table 2.** Parameters for training each neural network

Neural Network	FCN	SegNet	U-net
Dataset Composition	60% training / 40% testing		
Number of Iterations	11550	11550	42570
Batch Size	10	10	10
Elapsed Time	161 mins	143 mins	230 mins

### 3.2 Comparing Fully Convolutional Networks (FCN), SegNet, and U-net

**Fully Convolutional Networks (FCN):** In 2015, Long first utilized the fully convolutional network (FCN) to solve a semantic segmentation task by transforming image pixels into pixel classes [11]. Modified based on CNN, it only performs convolution (subsampling and upsampling)

and does not have fully connected layers. One of the advantages of the absence of the dense layer is the allowance of variation of input image size, which makes training data more diverse and applicable to void detection with various morphology. In Figure 7, FCN shows constant training progress during the first epoch and only minor adjustments when first initiating the network.

**SegNet:** Badrinarayanan designed a neural network (SegNet) particularly for semantic segmentation [12]. This network contains an encoder network engine and a corresponding decoder network classification layer, followed by a pixel-wise classification layer at the end. There are fully connected layers within the architecture; transferring from encoder to decoder is needed every time, meaning more concatenation and more memory will be occupied. The target application for this network was for scene understanding applications or large-scale images [12]. Therefore, patch size should be weighed — not too large to saturate GPU memory, nor too small to underfit the model.

**U-net:** U-net was released in 2015 and belonged to a variant of FCN. The motivation of the U-net was designed for biomedical image analysis; it has been widely used in other fields of semantic segmentation involving small-scale images, such as industrial defect detection, etc. U-net, similarly to FCN, has an encoder-decoder structure, in which the encoder is responsible for feature extraction.

### 3.2.1 Visual Inspection

One of the advantages of image analysis is that results can be visualized for human inspection. By overlaying labeled pixels of each class with the original image, the results of each neural network were compared with the ground truth labeling. As shown in Figure 8, each column represents the original image, the binary masked image, the ground truth, and one neural network: FCN, SegNet, and U-net, respectively. Every network has its gain and loss. FCN has the clearest boundary depiction of voids and has covered most of the significant voids in the ground truth image. SegNet over-covers most of the voids and does not contour their shape. It successfully identifies the area where the voids appear but cannot specify the location precisely. U-net performed better than FCN in identifying voids smaller than 10 x 10 pixels, however, the contour line of the voids area is not continuous, leaving small gaps when the shape of the void is irregular.

All three networks yielded areas of unclassified voids. The most frequently missed area was porosity with light color and unclear boundaries. Experts can define boundaries easily because the brain is more capable of processing object shapes. Depicting the boundary is the most challenging task for pixel-level semantic segmentation neural networks. We concluded that under visual assessment, FCN produces the best result out of the three networks by accurately characterizing the void integrity.

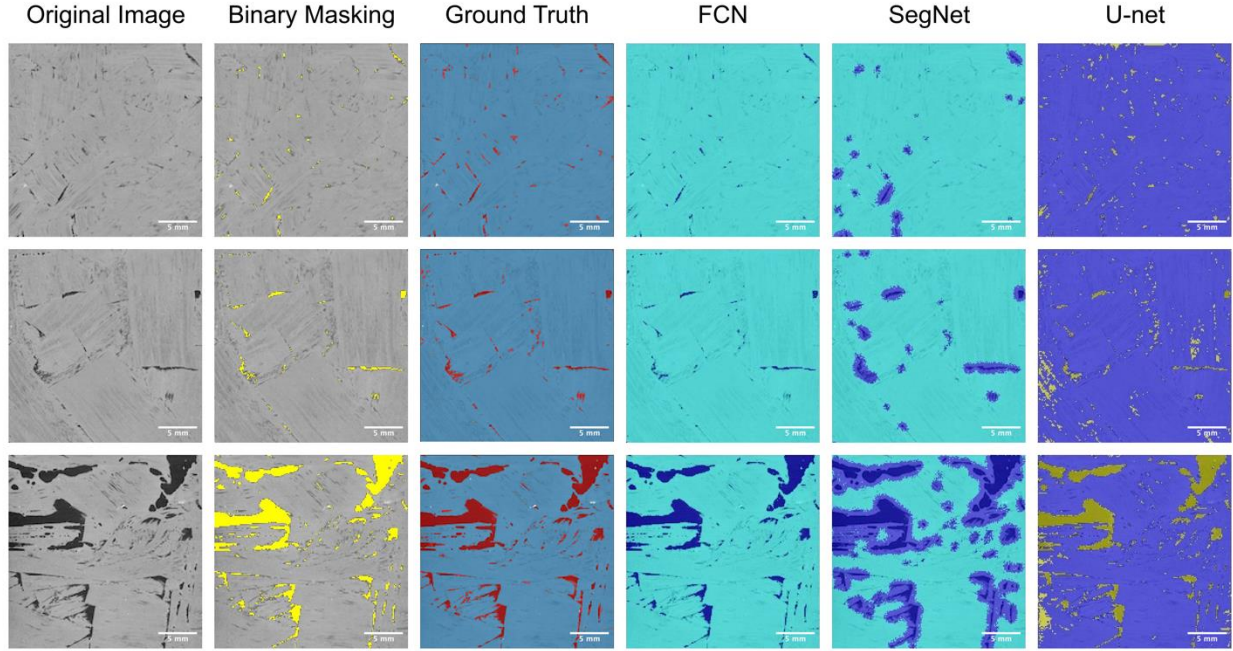


**Figure 8.** Visual comparison of segmentation results of FCN, SegNet, U-net, ground truth, binary masking, and original image.

### 3.2.2 Statistical Comparison

Statistical comparisons among the three networks were performed (Tables 3 and 4). Two metrics were introduced in evaluating each model's performance and gathered in Tables 3 and 4. Intersection over Union (IoU) score measures the accuracy of prediction based on corresponding ground truth. The greater the IoU, the greater the overlap between prediction and ground truth. A simple reference example of calculation, in this case, is illustrated in Figure 9 and Equation 1 below:

$$\text{IoU} = \frac{\text{Ground Truth} \cap \text{Prediction}}{\text{Ground Truth} \cup \text{Prediction}} = \frac{2}{13} = 0.15 \quad [1]$$

Boundary F1 (BF) score is a contour matching measurement between a predicted boundary of an object and the associated ground truth boundary [14]. The mean BF score is the calculated average of BF for each identified object. The following formula is used:

$$\text{BF score} = \frac{\text{Precision} * \text{Recall}}{\text{Recall} + \text{Precision}} * 2 \quad [2]$$

Accuracy is measured as the percentage of correctly identified pixels over the total number of pixels. Examining the tables, FCN is most accurate in correctly identifying pixel overall class and location. Global accuracy represents the ratio of correctly identified pixels over the total number of pixels of an image. This parameter enabled a quick estimation of a global view of the entire tomograph, as opposed to a pixel-to-pixel view. FCN has only 22 layers within a neural network, yielding the highest global accuracy and intersection over union (IoU) score in void content. This result matches with the visual inspection results that FCN have minor discontinuities



in boundary than SegNet or FCN. FCN has the greater potential for developing an autonomous void detection system with binary-masked input data with a relatively high BF score. SegNet ranks second, as its BF score is greater than U-net, indicating SegNet produces clearer contour shapes than U-net.

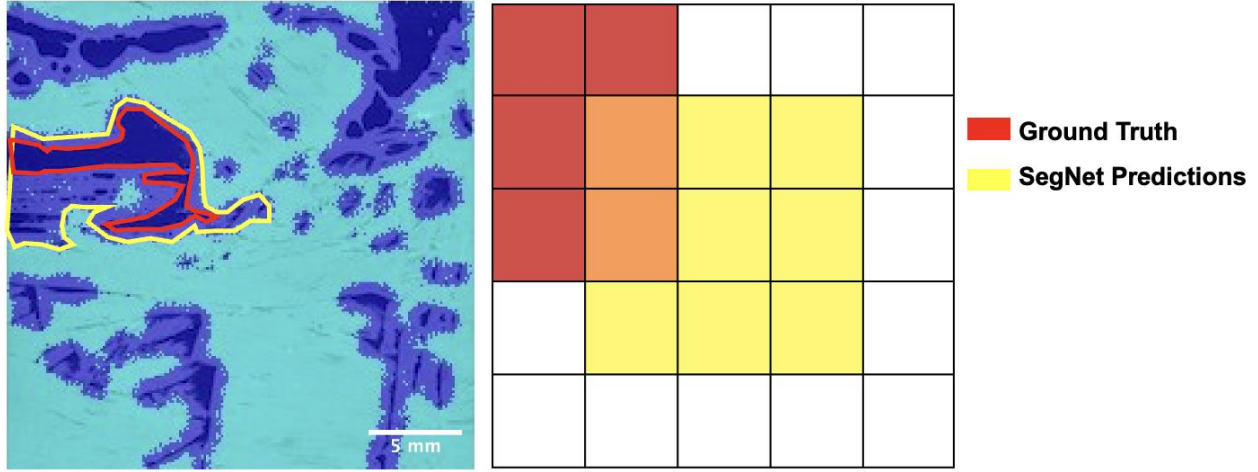


**Figure 9.** An example of the calculation of IoU.

Left: the sample output from SegNet.

Right: a straightforward representation of the process of calculating IoU.

**Table 3.** Segmentation Metrics for FCN, SegNet, and U-net.

Network Name	Global Accuracy	Mean Accuracy	Mean IoU	Weighted IoU	Mean BF Score
FCN	0.9320	0.4929	0.4701	0.8930	0.4399
SegNet	0.8258	0.4685	0.4219	0.7912	0.4316
U-net	0.9058	0.4908	0.4611	0.8682	0.4288

**Table 4.** Segmentation Metrics for FCN, SegNet, and U-net, separated by different labels.

Network Name	Label Area	Accuracy	IoU	MeanBFScore [1]
FCN	Void	0.0133	0.0082	0.1112
FCN	Panel	0.9724	0.9319	0.7686
SegNet	Void	0.0782	0.0186	0.1527
SegNet	Panel	0.8587	0.8252	0.7104
U-net	Void	0.0376	0.0165	0.1709
U-net	Panel	0.9440	0.9056	0.6867

### 3.3 Limitations of the Current Method

FCN, which yielded the most precise boundary and successfully classified most voids, was considered the best-performed model among the three neural networks in this work. However, by comparing the original images and the images that FCN classifies, Figure 8 visually suggested that FCN performed well only based on the binary masked image but neither the original images nor human-labeled. As the training input of models, binary masked labeling limits the accuracy of trained neural networks with an upper bound, making the classification results unprecise compared to the original image. Further study will develop better labeling solutions for training deep learning networks.

## 4. CONCLUSIONS

This work deployed MATLAB-based techniques to implement 3 neural networks for automatically identifying voids in micro-CT data of COSBs. The visual and statistical results demonstrate the potential of an autonomous void detection system with nearly no human intervention. FCN yielded a more accurate boundary depiction than the other two networks. Optimizing parameters within each neural network will undoubtedly reduce GPU memory and elapsed time.

The study illustrates approaches to the analysis of void content and provides efficient and autonomous solutions to void identification. Automation of analysis, particularly of volumetric images, can speed throughput and eliminate tedium. The analysis can be extended to the tasks of characterizing void morphology, spatial distribution, and even type.

Autonomous detection of voids can be applied to a wide range of materials other than composites. Added value will be gained from extracting more detailed information about porosity, including morphology and location, and coupling these outputs with micromechanical analysis of the effects on macroscopic performance. Autonomous analysis of volumetric images will also yield benefits when applied to studies of void evolution and the effects of process parameters/conditions.

1. Investigate boundary awareness and object localization of FCN and U-net when engaging larger and more complex tomography datasets in which most voids appear as interlaminar [19].
2. Optimize Fully Convolutional Network (FCN) by testing its performance with other open-source neural networks, e.g., U-net + VGG 16 introduced by Kopp et al., MIT in 2022 [14 - 18].
3. Generalize and escalate the detection system to serve different shapes and distribution of voids and voids in other material systems, e.g., the void analysis of honeycomb manufacturing.
4. Permit more types of 3-D and 4-D input data for the automated segmentation tools, allowing detailed analysis of voids morphology and their impact on mechanical properties.

## 5. REFERENCES

- [1] R. A. Smith. Composite Defects and Their Detection. Materials Science and Engineering. Vol. III. Encyclopedia of Life Support Systems (EOLSS). 2009.
- [2] Mahoor Mehdikhani, Larissa Gorbatikh, Ignaas Verpoest and Stepan V Lomov. Voids in fiber-reinforced polymer composites: A review on their formation, characteristics, and effects on mechanical performance. *Journal of Composite Materials*, 2019, Vol. 53(12) 1579–1669.
- [3] João M. Machado, João Manuel R.S. Tavares, Pedro P. Camanho, and Nuno Correia. Automatic void content assessment of composite laminates using a machine-learning approach. *Composite Structures*, Volume 288, 2022, 115383, ISSN 0263-8223.
- [4] B. Wei, K. Hao, X. S. Tang, and Y. Ding, “A new method using the convolutional neural network with compressive sensing for fabric defect classification based on small sample sizes,” *Textile Research Journal*, vol. 89, no. 17, pp. 3539–3555, Sep. 2019.
- [5] Karayiannis, Y.A., Stojanovic, R., Mitropoulos, P., Koulamas, C., Stouraitis, T., Koubias, S., Papadopoulos, G.: Defect detection and classification on web textile fabric using multiresolution decomposition and neural networks. In: *Electronics, Circuits and Systems*, 1999. Proceedings of ICECS’99. The 6th IEEE International Conference on. Vol. 2, pp. 765–768. IEEE (1999)

- [6] Kopaczka, M., Saggiomo, M., Güttler, M., Kielholz, K., Merhof, D. (2019). Detection and Classification of Faulty Weft Threads Using Both Feature-Based and Deep Convolutional Machine Learning Methods. In: De Marsico, M., di Baja, G., Fred, A. (eds) Pattern Recognition Applications and Methods. ICPRAM 2018. Lecture Notes in Computer Science, vol 11351. Springer, Cham.
- [7] Daniel Sammons, William P. Winfree, Eric Burke, et al. Segmenting delaminations in carbon fiber reinforced polymer composite CT using convolutional neural networks. AIP Conference Proceedings 1706, 110014 (2016); <https://doi.org/10.1063/1.4940585>.
- [8] Bo Cheng Jin, Xiaochen Li, Atul Jain, Carlos González, Javier LLorca, Steven Nutt. Optimizing microstructures and mechanical properties of composite oriented strand board from reused prepreg. *Composite Structures*, Volume 174, 2017, Pages 389-398, ISSN 0263-8223.
- [9] Jonathan Long, Evan Shelhamer, Trevor Darrell. Fully convolutional networks for semantic segmentation. 2015 IEEE Conference on Computer Vision and Pattern Recognition (CVPR), Year: 2015, Pages: 3431-3440.
- [10] V. Badrinarayanan, A. Kendall and R. Cipolla, "SegNet: A Deep Convolutional Encoder-Decoder Architecture for Image Segmentation," in *IEEE Transactions on Pattern Analysis and Machine Intelligence*, vol. 39, no. 12, pp. 2481-2495, 1 Dec. 2017, DOI: 10.1109/TPAMI.2016.2644615.
- [11] Shenli Pei, Kaifeng Wang, Jingjing Li, Yang Li, Danielle Zeng, Xuming Su, Xianghui Xiao, Hui Yang. Mechanical properties predict injection molded short/long carbon fiber reinforced polymer composites using micro X-ray computed tomography. *Composites Part A: Applied Science and Manufacturing*, Volume 130, 2020, 105732, ISSN 1359-835X.
- [12] MathWorks MATLAB, online Help Center, the topic of "bfscore." <https://www.mathworks.com/help/images/ref/bfscore.html>
- [13] Nikhil Mittal, Chidanand, Eswara Prasad. Carbon Fiber Reinforced Plastic (CFRP) Market by Raw Material (Polyacrylonitrile (PAN), Petroleum Pitch, and Others). Carbon Fiber Reinforced Plastic (CFRP) Market. Feb 2022.
- [14] Reed Kopp, Joshua Joseph, Xinchun Ni, Nicholas Roy, and Brian L. Wardle. Deep Learning Unlocks X-ray Microtomography Segmentation of Multiclass Microdamage in Heterogeneous Materials. *Advanced Material*, 2022, 2107817.
- [15] Reed Alan Kopp. X-ray Micro-Computed Tomography and Deep Learning Segmentation of Progressive Damage in Hierarchical Nanoengineered Carbon Fiber Composites. Massachusetts Institute of Technology. Department of Aeronautics and Astronautics. 2021.
- [16] Brian L. Wardle, Roberto Guzman de Villoria, Antonio Miravete, Southborough. Systems and methods for structural sensing. United States Patent, 2014.
- [17] Wardle B, et al., Fabrication and Characterization of Ultrahigh-Volume-Fraction Aligned Carbon Nanotube-Polymer Composites. *Advanced Materials*, vol. 20, pp. 2707-2714 (2008)
- [18] Dhimiter Bello, Brian L Wardle, Namiko Yamamoto, et al. Exposure to nanoscale particles and fibers during machining of hybrid advanced composites containing carbon nanotubes. *Journal of Nanoparticle Research*, Springer Netherlands, 11-1, 2009.
- [19] Maysam Shahedi, Anusha Devi T.T., James D. Dormer, Baowei Fei. A Study on U-Net Limitations in Object Localization and Image Segmentation. University of Texas at Dallas. SIIM 20 Virtual Meeting, 2020.